Influence of the first weld bead on strain and stress states in wire+arc additive manufacturing

Camille Cambon, Issam Bendaoud, Sébastien Rouquette, Fabien Soulié

INFLUENCE OF THE FIRST WELD BEAD ON STRAIN AND STRESS STATES IN WIRE+ARC ADDITIVE MANUFACTURING

C. CAMBON*, I. BENDAOUD*, S. ROUQUETTE* and F. SOULIE*

*LMGC, Univ. Montpellier, CNRS, Montpellier, France

ABSTRACT

WAAM (Wire+Arc Additive Manufacturing) allows manufacturing mechanical components by adding successive layers of molten metallic wire using electrical arc. The WAAM process, compared to other processes using metallic powders, presents some advantages such as: high deposition rate (2-4kg/hour), manufacturing of large scales components and cheaper industrial installations. WAAM is then an interesting candidate for manufacturing components often CNC machined. However, the main disadvantages of this process are: high surface roughness requiring a post machining, strains and stresses states generated during the deposition process [1]. A better understanding of the relation between the welding parameters and the state of stresses can contribute to minimize residual stresses, eventually in relation with a deposition strategy [2]. As a first approach, the effects of the first deposition of molten metal on the base plate is investigated. This work focuses on finite element method, based on Code Aster solver, with a nonlinear thermo-mechanical model. Concerning the thermal aspects, the GMAW heat input is modeled by a Gaussian distribution [3]. The temperature fields are used to solve the mechanical problem. The material behavior laws are assumed to be elastoplastic with different hardening configurations: no hardening, linear isotropic or kinematic hardening and non-linear isotropic hardening. Based on the results from these elastoplastic models, the influence of the hardening is presented.

Key-words: WAAM process, GMAW, Thermo-mechanical modeling, Residual stresses, Hardening

INTRODUCTION

Almost one century ago, in 1920, R. Baker patented a technique for manufacturing decorative objects in a similar way to the WAAM one [4]. Nowadays, WAAM technology has greatly improved to the point that metal manufacturers have a growing interest in this revolutionary manufacturing process. However, despite some interesting advantages, WAAM application fields still remain little diversified or limited to prototyping level. Indeed, WAAM manufactured parts can present structural defects partly due to the residual stresses resulting of the deposition thermal cycles. These residual stresses also contribute in the generation of significant distortions which may lead to inaccurate deformed parts. An example of this problem is given in figure 1. This sample was manufactured in our lab with sixteen layers of G3Si1 steel [5]. The deformation of the baseplate is mainly due to thermal effect. It appears from the first layer and the maximal out-of-plane displacement of the base plate edges can be up to 5 mm.

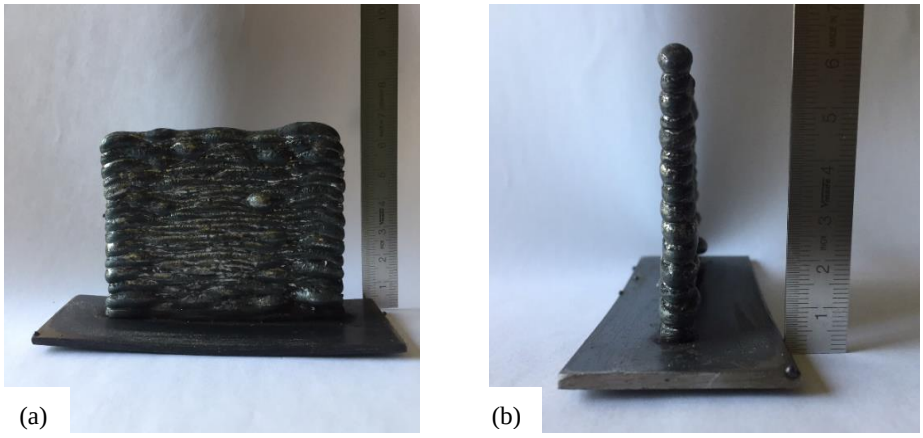

(a) (b)

Fig. 1 WAAM sample obtained with CMT process in LMGC facility. The thickness of the baseplate is 3 mm and 16 layers of G3Si1 steel were used to manufacture the sample: (a) front view, (b) side view.

The main objective of this scientific research is to understand residual stresses induced by WAAM process in order to lower it [6]. A Finite Element Analysis (FEA) associated to an experimental procedure are set up to get both distortions and residual stresses state. The present analysis is based on a thermomechanical weak coupling which considers only the influence of the thermal loading on the mechanical phenomena. The analysis is performed in two sequential steps. First, a thermal simulation is run in order to determine the temperature field generated by the welding torch. Secondly, this temperature field is used as an input data for the mechanical calculation of stress and strain states.

The numerical analysis is performed on a Stainless Steel (SS) 316L plate modelled in 2D under plane stress assumption (100 mm / 60 mm). The thermo-mechanical simulation is done with SalomeMeca software (Code Aster). The thermomechanical model is described in the first part of this work. Then, the results obtained at the end of each numerical analysis are presented. Finally, the influence of the hardening (linear, non-linear, isotropic, kinematic) on the numerical results, residual stresses and distortions, is discussed.

MODELLING

The WAAM technology uses a GMAW (Gas Metal Arc Welding) process for the deposition of metallic wire. GMAW is an electric arc-based welding process [7]. The heat generated from the electric arc allows melting the metallic wire. Modelling completely this process is extremely complicated as it involves electromagnetic, fluid flow (in the molten metal pool), heat transfers, metallurgical transformations and mechanical phenomena. The driving physic is the heat generated by the electrical arc. This study is limited to the effect of the deposition thermal cycle on the generation of strain and stress states in both the deposit and plate. Indeed, this process generates high thermally-induced residual stresses causing the formation of residual stresses and distortions. Neither metallurgical transformations are taken into consideration as the latent heat of phase change is generally smaller than the latent heat of fusion nor the effect of microstructure changes on the residual stresses that is assumed to be secondary.

A thorough thermal approach should include the arc plasma heat transfers and molten metal flows in the weld pool [8]. The weld pool surface is subjected to the action of arc pressure, gravity and surface tension and it is assumed to be in a static equilibrium. The effect of electromagnetic forces is neglected as the welding intensity is below 200 A [9]. The convection effects in the molten pool is considered by increasing the thermal conductivity value. An equivalent heat source is used for modelling the heat transfer between the arc plasma and the metallic work piece. Finally, half part of the work piece is considered since the weld is symmetrical along the joint centerline.

GENERAL ASSUMPTIONS

The thermal and mechanical studies have been performed under the following assumptions:

- 2D geometry with symmetry axis,
- heat conduction transfer with temperature dependent thermophysical properties,
- Lagrangian reference coordinate system with a moving heat source,
- a Gaussian mathematical expression describes the heat source,
- the convection effect in the weld pool is modelled with an increased value of thermal conductivity,
- the mechanical problem is solved once the thermal analysis has been done (weak coupling),
- material mechanical properties are also temperature dependent,
- no metallurgical transformations,
- 2D plane stress assumption,
- no transverse displacement along the symmetry axis (Ox) and no displacement (in both directions) along the (Oy) axis at x=0 mm (see Fig. 2),
- the two other boundaries are condition-free.

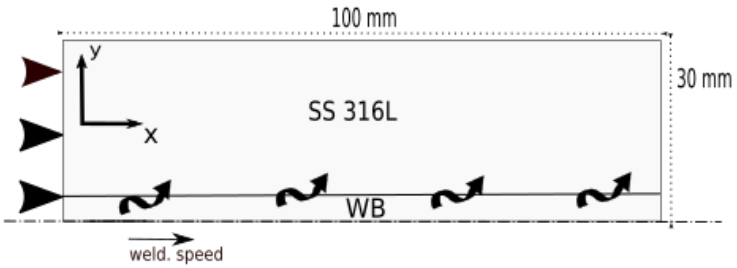

Fig. 2 Studied geometry: a thin plate of size 100 x 30 x 3 mm with prescribed displacements on its left (black triangles).

HEAT CONDUCTION AND THERMOPHYSICAL PROPERTIES

Let's consider a domain Ω defined by the top plate face. The considered geometry is 2-Dimensional as the plate thickness is lower than the two other dimensions. The heat transfer through the thickness is neglected. The plate is scanned with a mobile heat source (GMAW torch) on its center so half part of the domain is investigated. A Lagrangian reference coordinate system (O,x,y) is defined from a corner of the domain on the symmetry axis. The applied thermal loading Q is a heat source defined with a Gaussian mathematical formulation (Eqn. (3)). The temperature field T(x,y,t) is the solution of equation system defined with the heat conduction equation with no internal heat production (Eqn. (1)), associated boundary conditions and initial condition (Eqn. (2)).

$$\rho(T)c_p(T)\frac{\partial T}{\partial t}=\lambda(T)\nabla^2(T)+Q \tag{1}$$

Where
ρ is the densité (kg m^{-3}),
c_p is the specific heat (J kg^{-1} K^{-1}),
λ is the thermal conductivity (W m^{-1} K^{-1}) and,
Q is the heat source (W m^{-2}).

This nonlinear second-order PDE (Partial Differential Equation) cannot be solved uniquely without defining the boundary conditions and an initial condition. The associated boundary and initial conditions are:

$$-\lambda\frac{\partial T}{\partial n}=h(T-T_0)+\varepsilon\sigma\left(T^4-T_0^4\right)+q(x,y,t) \tag{2}$$

Where
n is the outside normal,
q is the surface source (W m^{-2}),
h is the convective exchange coefficient (W m^{-2} K^{-1}),
σ is the Stefan-Boltzman constant ($\sigma = 5.68\ 10^8$ J K^{-4} m^{-2} s^{-1}),
ε is the metal emissivity and,
T_0 is the ambient temperature (K) considered as initial condition $T(x,y,t=t_0)=T_0$.

The absorbed heat (from the electric arc) is modelled with an equivalent heat source described with a Gaussian mathematical expression as follows:

$$q(x,y,t)=\frac{3\eta UI}{\pi R_0 e}\exp\left(-3\frac{(x-x_0-V_s t)^2+y^2}{R_0^2}\right) \tag{3}$$

Where
η is the process efficiency,
U is the welding voltage (V),
I is the welding intensity (A),
R_0 is the Gaussian distribution of the heat source (m),
e is the thickness of the plate (m) and,
V_s is the welding velocity (m s^{-1}).

The thermophysical properties of SS 316L are assumed to be temperature dependent (see Table 2 in appendices) The enthalpy formulation is employed to solve the heat equation problem.

SalomeMeca software offers the possibility of using an enthalpic formulation for the heat conduction equation. The enthalpy function β(T) is defined as the product of the density ρ with the specific heat C_p. The

enthalpic formulation is especially useful when important amount of latent heat is considered such as fusion phenomena. The enthalpic formulation provides a smoother and monotonic temperature dependent variable than the specific heat C_p which exhibits an important peak nearby the temperature of fusion. This huge change in C_p values is generally the cause of either numerical convergence problems or the latent heat of fusion is not considered according the chosen time step of the simulation. The enthalpy function is defined as follows:

$$\beta(T)=\int_{T_0}^{T}\rho C_p(u)du \tag{4}$$

Let's remember that the thermal conductivity is multiplied by 2 in the molten pool. This value is set to 60 $W.m^{-1}K^{-1}$ as it is shown in table 1. This numerical artifice is often used to reproduce the convection in the molten pool in order to get a suitable weld pool length.

The temperature range of fusion for the SS 316L is fixed to occur between 1400°C and 1500°C with a latent heat value of 2.0 10^9 $J.m^{-3}$[10]. The enthalpy curve for the SS 316L is presented in Fig. 3.

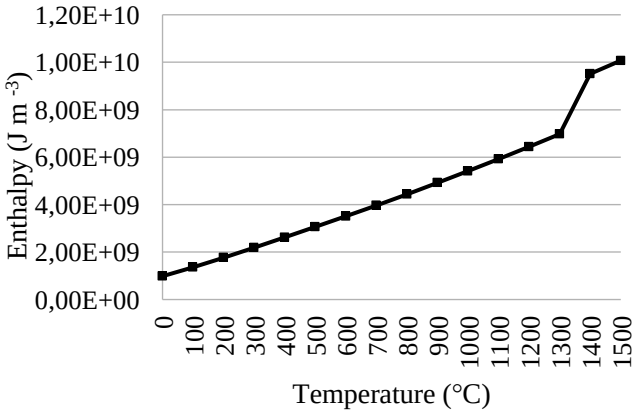

Fig. 3 Evolution of the Enthalpy with regards to the temperature for SS 316L.

MECHANICAL MODEL

A transient mechanical analysis is performed in order to calculate the strain and stress responses to the thermal cycle previously presented. Let's remember that the thermal analysis results are used as thermal loading into the mechanical analysis. The thermal and mechanical analysis are performed in a one-way manner (weak coupling). A nonlinear static solver is used. The material behavior law is assumed to be elastoplastic. The influence of viscous phenomena is neglected. Four different types of hardening are investigated in order to observe their effect on the final strain and stress fields:

- Linear isotropic hardening
- Non-linear isotropic hardening
- Zero hardening (perfectly elastoplastic)
- Linear kinematic hardening

All these analyses are run under large deformations assumption with the "PETIT_REAC" solver of SalomeMeca/Code_Aster software. "PETIT_REAC" solver is based on a geometry update (position of nodes) at each Newton iteration. So, several geometry updates are performed for each time step of the mechanical calculation. Apart this geometry update, the solver works like for the small deformations [11] [12]. The "PETIT_REAC" solver is well suited for large deformations if rotation motions are small, the elastic strain is lower than the plastic strain, the material behavior law is isotropic and for smaller Newton iterations.

Governing equations

At each time step, the mechanical problem must verify the equilibrium equation:

$$\mathrm{div}(\sigma)+f_{volume}=0. \quad (5)$$

Furthermore, under small deformations hypothesis, the strain tensor is defined according to the displacements:

$$\Delta\varepsilon=\frac{1}{2}(\boldsymbol{\nabla}_{\boldsymbol{\Omega i}}(\Delta\mathbf{u})+\boldsymbol{\nabla}^{\mathbf{T}}_{\boldsymbol{\Omega i}}(\Delta\mathbf{u})), \quad (6)$$

With Ω_i the updated configuration.

Under the assumption of small strains and considering an elastoplastic model, the strains decomposition at any time is formulated as follows:

$$\boldsymbol{\varepsilon}(t)=\boldsymbol{\varepsilon}^{e}(t)+\boldsymbol{\varepsilon}^{th}(t)+\boldsymbol{\varepsilon}^{p}(t), \quad (7)$$

With

$$\varepsilon^{e}(t)=A^{-1}\big(T(t)\big)\sigma(t), \quad (8)$$

and

$$\varepsilon^{th}(t)=\alpha\big(T(t)\big)(T(t)-T_{ref})\mathrm{Id}. \quad (9)$$

A is the elasticity tensor which depends on the temperature at time t. The coefficient α is the average coefficient of thermal expansion depending in terms of a reference temperature T_{ref} for which the thermal expansion is zero.

Finally, the discretized relation is:

$$\Delta\varepsilon=\Delta\varepsilon^{p}+\Delta\big(A^{-1}\sigma\big)+\Delta\varepsilon^{th} \quad (10)$$

Mechanical properties

The mechanical analysis is strongly nonlinear due to both the transient thermal loading and the temperature dependence of the SS 316L mechanical properties. SS 316L yield strength and Young modulus decrease with the increase of temperature as it is shown in Table 2 and Fig. 13 in appendices. In order to cancel the stress in the molten pool, both yield strength and Young modulus have been fixed to low values (beyond T=1400°C).

Moreover, in order to cancel the cumulative plastic strains in the molten pool, a multiplicative function describing the hardening restoration is defined as follow [14]:

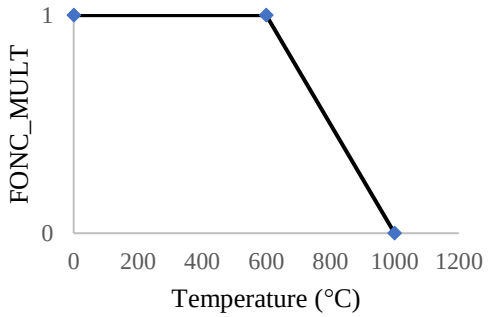

Fig. 4 Multiplicative function of hardening restoration for SS 316L.

Boundary Conditions

The plate is fixed on one side along the (Oy) direction as it is shown in Fig. 5 (full black triangles). All the nodes have a prescribed displacement in both x and y direction (DX=0 and DY=0). Furthermore, the welding line, (Ox direction), has prescribed displacement in the y direction (DY=0) in order to satisfy the symmetry condition.

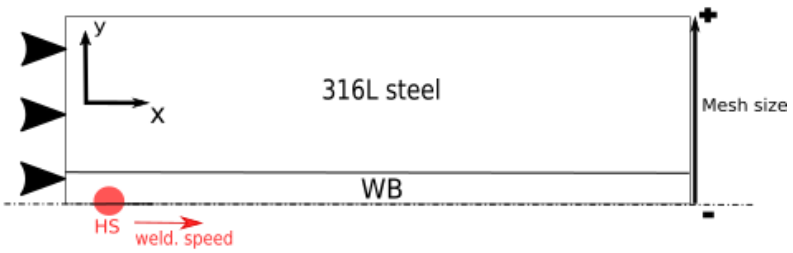

Fig. 5 Mechanical boundary conditions.

RESULTS AND DISCUSSION

CALCULATED TEMPERATURE FIELD

The average electric parameters are U=12 V; I=120 A. The process efficiency is fixed to η=0.8 as it is classical for a GMAW process. The welding speed is set to V_s=5 mm s^{-1}. The last parameters which are required in the Gaussian heat flux expression are chosen equal to R_0=3 mm for the Gaussian distribution and e=3 mm for the plate thickness. The Gaussian radius was roughly estimated in order to get a weld pool half-width of about 2 mm as observed experimentally. The total simulation duration is about 36.8 s defined as 0.8 s for the initiation followed of 16 s for the heat flux to scan the 80 mm of the plate and 20 s of cooling. The meshgrid used for the thermal simulation consists in 12090 quadrangle elements defined with 11546 nodes. The minimum element size is 0.2 mm in the weld bead and increases progressively far from the weld bead zone. The calculation is performed with a direct solver. The total CPU time consumed is 3725 s (~1h) for a time step of 0.04 s with a smaller time step of 0.008 s at the initiation of the heat source. The results of the thermal simulation are presented in Fig. 6 and 7.

In Fig. 6, the calculated temperature field is presented at time t=8 s. The shape of the molten pool is delimited with the black line corresponding to the isotherm T=1400°C. The molten pool exhibits a classic elongated shape. Its dimensions are 5 mm long by 2 mm half-width. The part of the plate in front of the source is not yet affected by the heating and it remains equal to the initial temperature. The thermal gradient in front of the heat source is important as it is commonly observed in welding experiment. This is due to the low thermal diffusivity (ratio $\lambda / (\rho.C_p)$) of SS 316L which takes values between 3,89x10^{-6} m^2 s^{-1} to 5,64x10^{-6} m^2 s^{-1} between 20°C and 1200°C. The heat propagates slower than the heat source motion so a high thermal gradient is produced in front of the heat source. At the rear of the heat source, the heat propagates towards the width by conduction. The boundary located at x=0 mm is slightly heated by conduction as the heat source started 10 mm further. A maximum temperature of 1790°C is reached inside the molten pool. The isotherm defining the weld pool shape exhibits a perpendicular tangential derivative on the symmetry axis. This behaviour is due to the symmetry condition imposed on this boundary (homogenous Neumann condition). The computation of Biot number (Bi = h.L/λ with h the convective exchange coefficient, L is a characteristic length and λ is the thermal conductivity) leads to a value between 0,003 and 0,0015 in the temperature range 20°C-1200°C (with h= 15 W m^{-2} K^{-1} and L is equal to the plate thickness). For Biot values inferior to 0.1, it can be assumed that the temperature field is almost the same through the plate thickness.

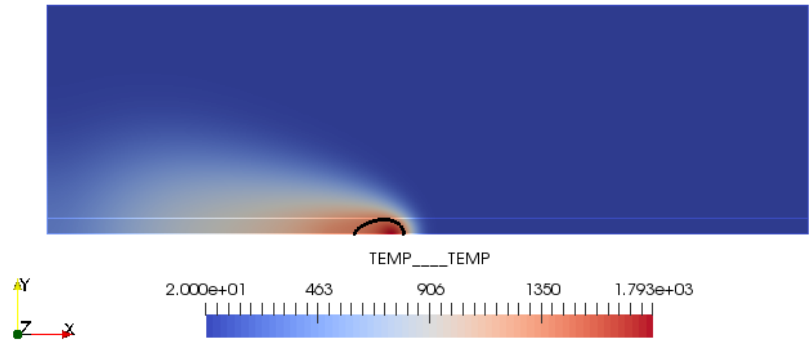

Fig. 6 Temperature field (°C) at time t= 8 s. The weld pool shape is defined by the melting isotherm T_f=1400°C (black line).

The temporal evolution of the temperature at time t=8 s on the symmetry axis (see Fig. 7.a) is reported in Fig. 7.b. The temperature history is divided in four parts. Firstly, the temperature remains equal to the initial condition till the heat source comes over its position. Secondly, the heating rate increases hugely, about 1275°C s^{-1}, as the temperature rises from 20°C to 1790°C in about 1.5 s. Then the material cools down quickly from 1790°C to 1400°C with a cooling rate similar to the heating rate. At 1400°C, the cooling rate slows down to 80°C s^{-1}. This is due to the release of the latent heat of fusion. Once the material is totally solidified, the cooling rate decreases from 200°C s^{-1} (at t~11.5 s) to 10°C s^{-1} at the end of the computation (t~37 s). The plate has not reached the room temperature after 20 s of heat flux extinction. The average temperature of the plate is between 400°C and 500°C after 20 s of cooling time. At a cooling rate of 10°C s^{-1}, it would take 40 to 50 more seconds to reach the room temperature. Experimentally, it is extremely difficult to get thermal data inside the weld pool and its vicinity. Nevertheless, the weld pool shape and temperature field are in good agreement with some data found in the literature [15].

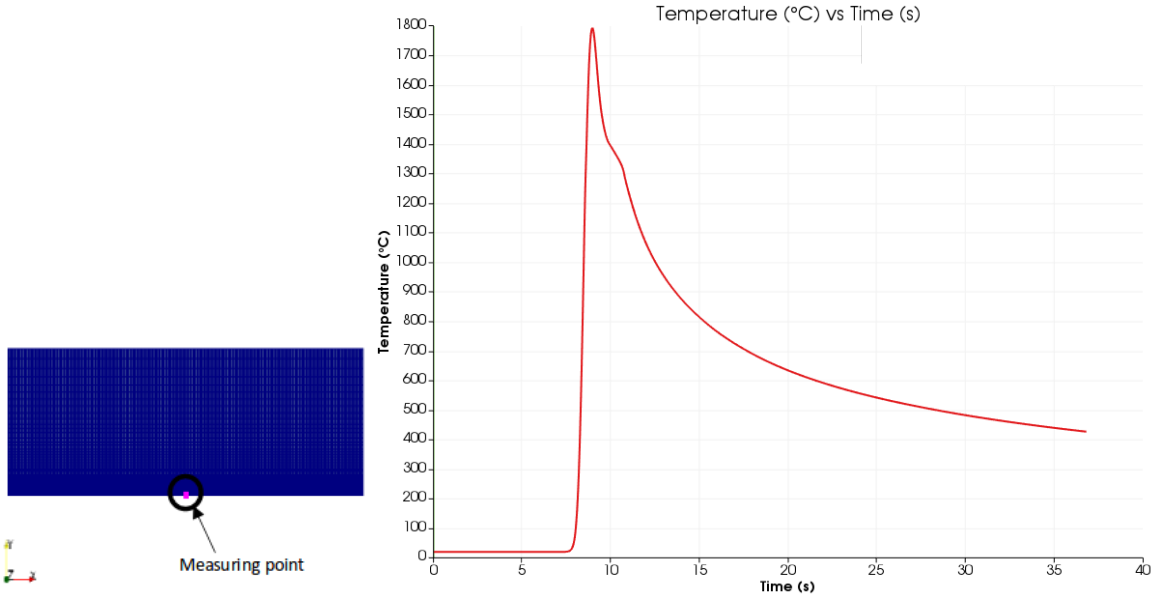

(a) (b)

Fig. 7 Time evolution of the temperature (b) for an arbitrary point on the symmetry axis (a).

This temperature results are used in the mechanical computation in order to predict the residual stresses generated by the heat flux passage. The effect of this thermal cycle on the residual stresses is presented in the next section.

STRESS FIELDS

For the mechanical computation, the mesh is composed by 7290 quadrangle elements and 6946 nodes. Like the thermal analysis, a mesh refinement is made in the weld bead zone with a mesh element size of 0.2 mm. The computation is performed with a direct solver. The CPU time consumed for each analysis is nearly the same, about 40 000 s (~11 h) for a time step of 5.10^{-4} s.

The longitudinal stress field and evolution along the longitudinal and transverse directions are presented respectively in Fig. 9, 10, 11 and 12. The presented results in Fig. 9, 11 and 12 is obtained at the final time of the mechanical computation then after 20 s of cooling. Fig. 10 presents the longitudinal stress evolution at time t=8 s along two longitudinal axis L1 and L2 (see Fig. 8) respectively situated at 1mm and 10 mm from symmetry axis (Ox). Let's remember that the SS 316L is supposed to be elastoplastic with hardening. Four hardening cases have been investigated: perfectly plastic, linear isotropic, nonlinear isotropic and linear kinematic.

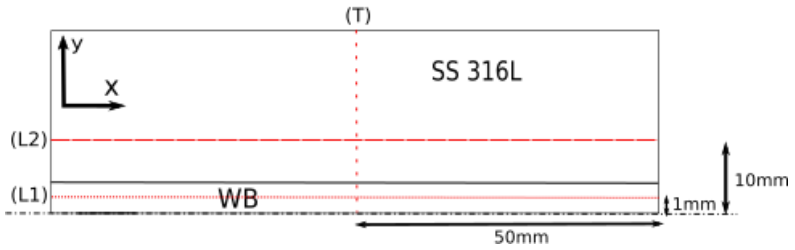

Fig. 8 Position of observation lines: 2 lines L1 and L2 are parallel and respectively located at 1 m and 10 mm from to the symmetry axis (Ox). The third line L3 is located at y=50 mm and perpendicular to the symmetry axis (Ox).

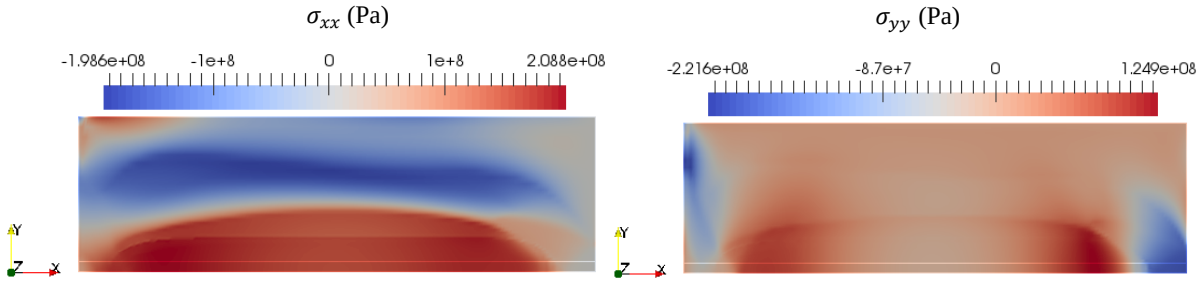

(a) (b)

Fig. 9 Longitudinal stress (σ_{xx} for (a)) and transverse stress (σ_{yy} for (b)) fields at t=t_{final} (~37 s) under elastoplastic behavior with linear isotropic hardening (Pa).

The longitudinal stress (σ_{xx}) field is tensile between the starting and ending points of the weld path as we can see in Fig. 9.a. The longitudinal stress has a homogenous value along the weld bead (around +200 MPa). This longitudinal stress field has a classic distribution. Inside the molten pool, the stress must be equal to zero as it is observed experimentally (a numerical artifice cancels the stress when the temperature is greater than 1400°C). Thus, during the solidification, the material shrinkage leads to tensile stress at the back of the weld pool as we can see in Fig. 9.a.

Transverse stress (σ_{yy}) is tensile in the domain defined by the weld bead and heat affected zone. The transverse stress is equal to zero on the free lateral boundary (y=30 mm). Another edge effect is visible on the fixed boundary (x=0 mm); the transverse stress is under compression due to the condition of prescribed displacements in both directions.

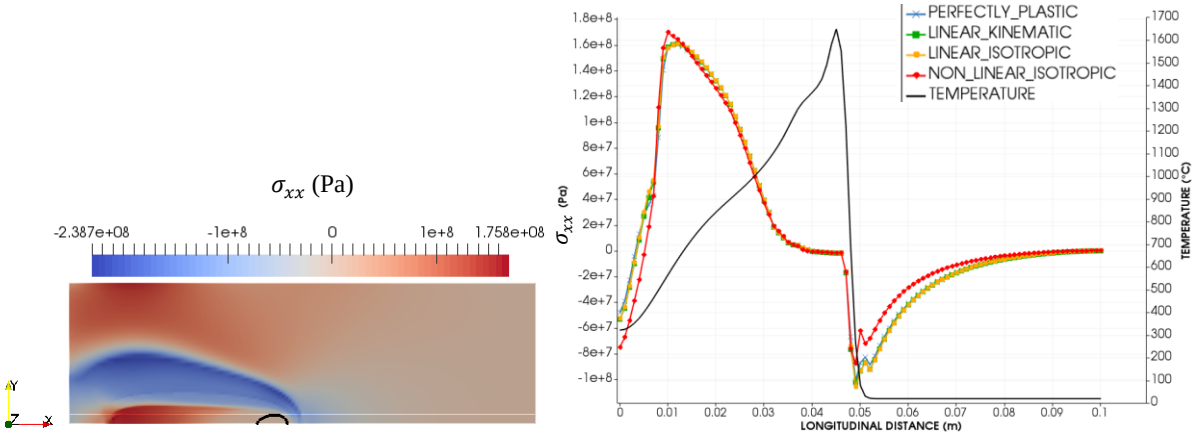

(a) (b)

Fig. 10 At t=8 s, along L1: (a) Longitudinal stresses (σ_{xx}) field at t=8 s. (b): Evolution of the longitudinal stresses (σ_{xx}) for four hardening configurations (left vertical axis in Pa) and temperature distribution (right vertical axis in °C).

Fig. 10.a and 10.b present the longitudinal stress field when the heat source is located at x~50 mm (t~8 s). The evolution of longitudinal stress along L1 line is presented as well as the temperature history. In front of the heat source (x>50 mm), the zone is under compression due to dilatation effects because of the high temperature

difference in few millimeters. The temperature rises suddenly from 20°C to 1700°C. The stress values are equal to zero inside the molten pool because the cut-off temperature imposed on the material properties for canceling the stress ($T_{cut\text{-}off}$ = 1400°C). Once the temperature, at the back of the heat source, goes below $T_{cuf\text{-}off}$, the longitudinal stress goes from 0 MPa to reach 150-160 MPa. At x=10 mm, the longitudinal stress has not yet reached its maximum value as shown in Fig. 11.b (about 220 MPa at $t=t_{final}$).

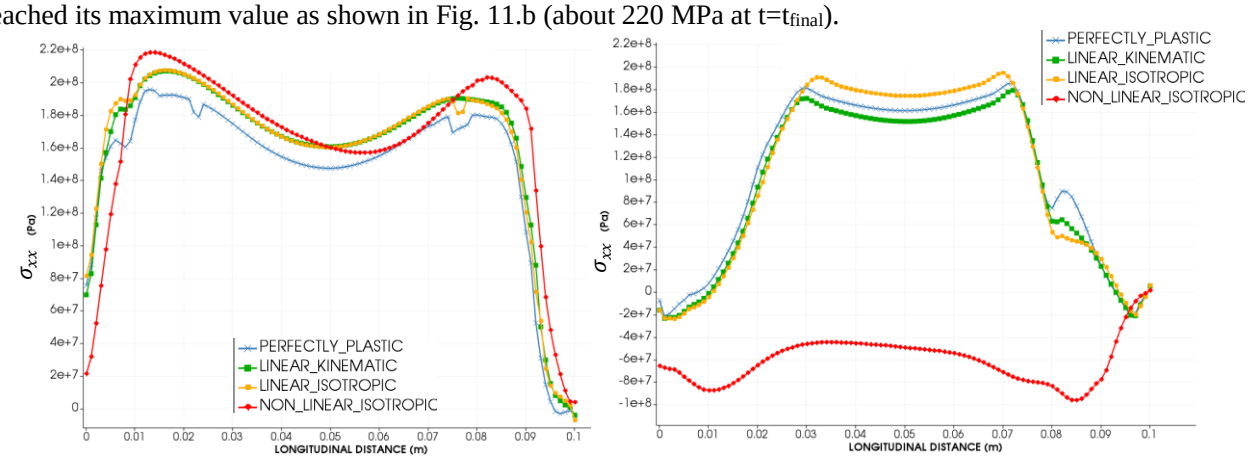

(a) (b)

Fig. 11 Evolution of longitudinal residual stress (σ_{xx}) along L1 line (a) and L2 line (b) parallel to the weld bead and located respectively at 1 mm and 10 mm from the symmetry axis.

As mentioned for the longitudinal stress field, the longitudinal stress is cancelled on the free boundary, at x=100 mm. The longitudinal stress is slightly tensile on the fixed boundary (x=0 mm) because of the boundary condition applied here: no displacement in both directions, see Fig. 11.a. The longitudinal stress reaches two peaks values (~220 MPa) at the beginning of weld path (x=10 mm) and at its end at x=90 mm this is due to the plate stiffness before the starting and after the ending points. The minimum value is reached at the plate middle with 160 MPa. At 10 mm from the symmetry axis, the longitudinal stress is still tensile and high with a homogenous value of 160 MPa between 30 mm < x < 80 mm, Fig. 11.b. All the studied hardening led to the same residual stress field and longitudinal distribution except for the nonlinear isotropic hardening case. The nonlinear isotropic hardening led to a narrower tensile zone for the longitudinal stress. Fig. 12.a shows that the longitudinal stress is tensile (about160 MPa) over 6-7 mm before decreasing and reaching a minimum value of -140 MPa at 12-13 mm from symmetry axis. The three other cases: perfectly plastic, linear isotropic and kinematic hardening led to a wider tensile zone, till 12 from symmetry axis and the minimum value is -200 MPa and it is reached about 20 mm from symmetry axis. The thermal loading is the same for the four studied cases. It seems that the nonlinear isotropic hardening leads to a narrower tensile zone (for σ_{xx}) and the compressive value is lower as well.

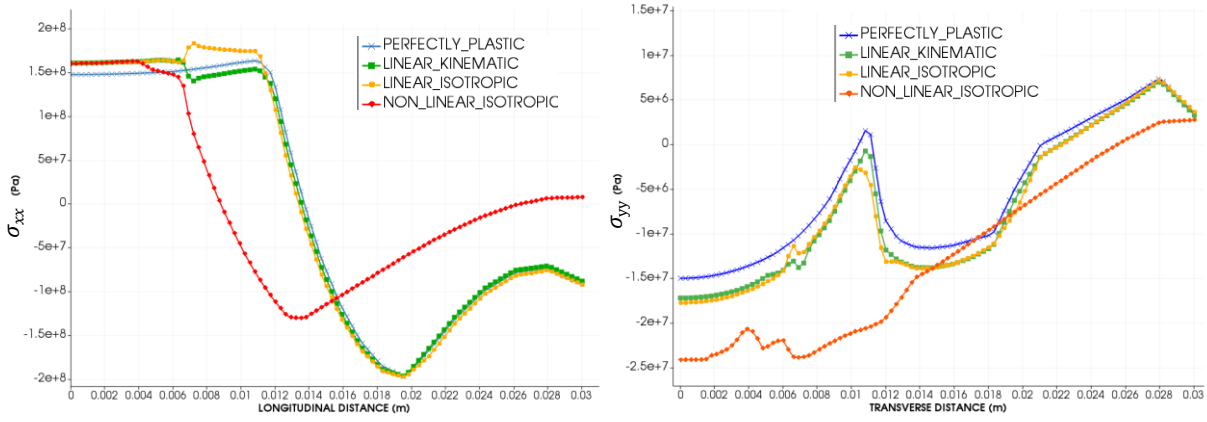

(a) (b)

Fig. 12 Evolution of longitudinal residual stress σ_{xx} (a) and transverse residual stress σ_{yy} (b) along a transverse line to the weld bead and located at x=50 mm.

Fig. 12.a presents a classical longitudinal stress distribution along a perpendicular direction to welding path. The weld bead and heat affected zones are tensile followed to a compression zone with a peak value of -200 MPa. As the plate width is quite narrow, this compressive longitudinal stress remains quite high with a value of about -100 MPa on the lateral boundary (y=30 mm). The calculated transverse stress at the plate middle (y=50mm) is more than 10 times lower than the longitudinal one. At this position of the weld bead, the stress field looks like an uniaxial loading as it is shown in Fig. 9.b. The transverse stress is high at the beginning and end of the weld bead probably due to the plate stiffness. The σ_{xx} and σ_{yy} residual stresses fields along transverse axis are in accordance with strain gauges and neutron diffraction measurements [16].

CONLUSION AND PROSPECTS

A thermo-mechanical analysis was conducted in order to appreciate the stress distribution induced by WAAM process. As a first approach, only the first weld bead is considered to evaluate the level of distortion and residual stresses that could affect the WAAM process during the successive deposition. The thermo-mechanical simulations were done with SalomeMeca software (Code Aster). The thermo-mechanical model is elastoplastic type with different hardening configurations (linear, non-linear, isotropic, kinematic).

The magnitude and distribution of residual stresses are very similar for all the types of hardening, both on longitudinal and transverse sections. Only the non-linear hardening presents some discrepancies.

The obtained differences are probably due to the nonlinear mechanical management by the solver. Nevertheless, the global behavior and the maximal values of stresses are nearly the same for all the hardening configurations.

The management of several layers deposition for thermomechanical analysis is in progress. It will be carried out in relation with an experimental study conducted in similar conditions. The experimental data obtained in our lab facility are both thermal data (temperature histories with thermocouples) and mechanical data (displacements and strains).

APPENDICES AND ACKNOWLEDGEMENTS

Table 1 Thermophysical properties of SS 316L [13].

Temperature (°C)	Conductivity ($W\ m^{-1}\ K^{-1}$)	Enthalpy ($J\ m^{-3}$)
0		9.8310^{8}
20	14	
100	15.2	$1.36\ 10^{9}$
200	16.6	$1.76\ 10^{9}$
300	17.9	$2.19\ 10^{9}$
400	19	$2.62\ 10^{9}$
500	20.6	$3.06\ 10^{9}$
600	21.8	$3.51\ 10^{9}$
700	23.1	$3.96\ 10^{9}$
800	24.3	$4.43\ 10^{9}$
900	26	$4.92\ 10^{9}$
1000	27.3	$5.42\ 10^{9}$
1100		$5.92\ 10^{9}$
1200	29.9	$6.44\ 10^{9}$
1300		$6.97\ 10^{9}$
1400	60.0	$9.51\ 10^{9}$
1500		$1.01\ 10^{10}$

Table 2 Mechanical properties of SS 316L [13].

Temperature (°C)	Young Modulus E (10^6Pa)	Yield Strength R_e (10^6Pa)	Coefficient of thermal expansion α (10^{-5})	Tangent modulus of elasticity E_T (10^6Pa)
20	197 000	287	1.55	2400
100	191 500	237	1.60	
200	184 000	198		
300	176 500	172	1.71	
400	168 000	157	1.75	
500	160 000	151		
600	151 500	145	1.84	
700	142 500	136	1.87	2400
800	130 000	127	1.90	2350
900	108 000	115		1500
1000	81 500	79	1.94	800
1100	32 000	38		725
1200	7 400	24		150
1300		18		10
1400		2	1.96	

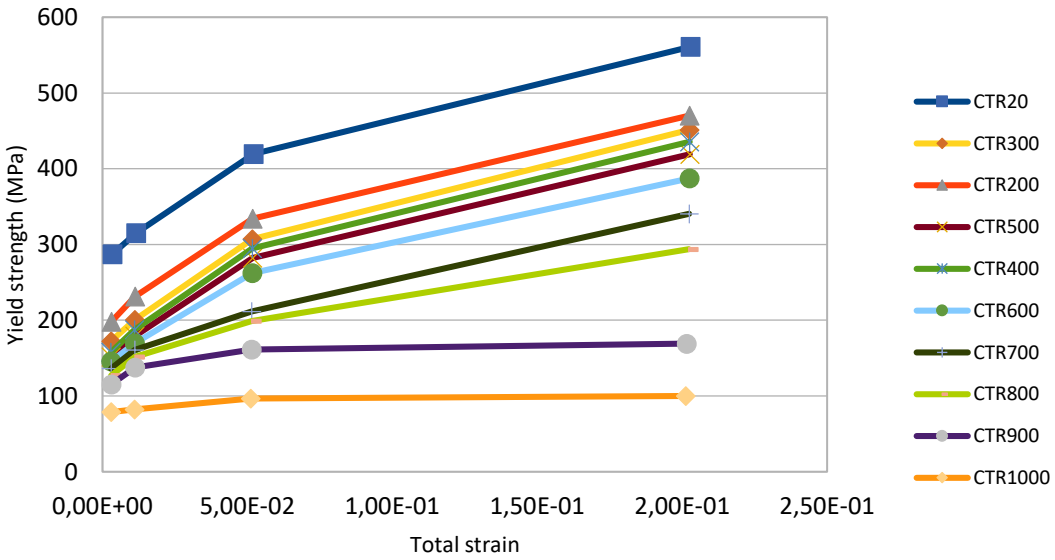

Fig. 13 Traction curves of SS 316L [13].

References

[1] D. DING, Z. PAN, D. CUIURI, H. LI: 'Wire-feed additive manufacturing of metal components: technologies, developments and future interests', *The International Journal of Advanced Manufacturing Technology 81*, University of Wollongong Northfield Ave, pp. 465-481, 2015.

[2] T. MUKHERJEE, W. ZHANG, T. DEBROY: 'An improved prediction of residual stresses and distortion in additive manufacturing', *Computational Materials Science 126*, The Pennsylvania State University, pp. 360-372, 2017.
[3] F. MONTEVECCHI, G. VENTURINI, A. SCIPPA, G. CAMPATELLI.: 'Finite Element modelling of Wire -Arc-Additive-Manufacturing process', *Procedia CIRP 55*, University of Firenze, pp. 109-114, 2016.
[4] R. BAKER: 'Method of Making Decorative Articles', *US Patent 1533,300*, filed November 12, 1920, patented 14th April, 1925.
[5] L. CORONA GALVAN : *Prototypage rapide de pièces en acier : étude du dépôt de matière et d'énergie lors de la fusion à l'arc d'un fil par le procédé MIG-CMT*, thesis, University of Montpellier, 2018
[6] L.D. COZZOLINO, H.E. COULES, P.A. COLEGROVE, S. WEN: 'Investigation of post-weld rolling methods to reduce residual stress and distortion', *Journal of Materials Processing Technology 247*, Cranfield University, pp. 234-256, 2017.
[7] J-P. PLANCKAERT : *Modélisation du soudage MIG/MAG en mode short-arc*, thesis, Henri Poincaré University, 2008.
[8] M.C. NGUYEN : *Modélisation et simulation multiphysique du bain de fusion en soudage à l'arc TIG*, thesis, Ecole polytechnique universitaire de Marseille, 2015.
[9] S. ROKHLIN, A. GUU: 'A study of arc force, pool depression, and weld penetration during gas tungsten arc welding', *Welding Journal 72:8*, The Ohio State University, pp. 381-390, 1993
[10] F.X TISSOT : *Etude phénoménologique et modélisation du comportement du bain de fusion en soudage TIG en vue d'une application au contrôle du procédé*, thesis, University of Aix-Marseille I
[11] D. HABOUSSA : 'Intégration des relations de comportement élasto-plastique de Von Mises', *Code_Aster Documentation*, R5.03.02, 2005
[12] E. LORENTZ: 'Modelling elasto (visco) plastic with isotropic work hardening in great deformations', *Code_Aster Documentation*, R5.03.21, 2013
[13] L. DEPRADEUX : *Simulation numérique du soudage-acier 316L Validation sur cas tests de complexité croissante*, thesis, L'Institut National des Sciences Appliquées de Lyon, 2004
[14] S. HENDILI : 'HSNV140 - Thermo-plasticité avec restauration d'écrouissage : essai de dilatométrie bloquée', *Code_Aster Documentation*, V7.22.140, 2016
[15] H. SCHOPP, A. SPERL, R. KOSAKOV, G. GOTT, D. UHRLANDT, G. WILHELM: 'Temperature and emissivity determination of liquid steel S235', *Journal of Physics D: Applied Physics 45*, INP-Greifswald, 9pp, 2012
[16] H.E. COULES, L.D. COZZOLINO, P. COLEGROVE, S. GANGULY, S. WEN, T. PIRLING: 'Residual strain measurement for arc welding and localised high-pressure rolling using resistance gauges and neutron diffraction', *Journal of Strain Analysis for Engineering Design 47*, University of Bristol, pp. 576-586, 2012